

# Adaptive stepsize forward–backward pursuit and acoustic emission-based health state assessment of high-speed train bearings

Defu Han<sup>1,2</sup>, Hongyuan Qi<sup>1,2</sup>, ShuangXin Wang<sup>1</sup>, Dongming Hou<sup>3,4</sup> and Cuiping Wang<sup>1,2</sup>

## Abstract

Compressed sensing (CS) is a promising tool for data compression reconstruction. However, fault diagnosis methods for high-speed train bearings based on CS and acoustic emission (AE) technologies have not been reported yet. Notably, the accuracy and speed of CS two-stage reconstruction methods are affected and restricted by prior initial conditions. Therefore, this article proposes adaptive dynamic thresholds applicable to adaptive stepsize forward–backward pursuit (ASFBP), and bearing health state assessment method. First, the adaptive dynamic thresholds for atom selection and deletion are constructed based on the residual feedback mechanism and the atom quality distribution law, which enables ASFBP to realize high-precision rapid reconstruction of signal without any atom priori initial conditions. Second, the initial dictionary length is improved based on the AE hit characteristics. Furthermore, a damage state comprehensive evaluation index (DSCEI) is established using principal component analysis based on AE time-domain hit parameters and compression-domain energy parameter. Compared with the kurtosis index and permutation entropy index, the DSCEI demonstrates better monotonicity and stability in the quantitative evaluation of high-speed train bearing condition. Finally, the validity and stability of the method are verified by testing under complex test conditions resembling actual high-speed train lines, providing valuable insights for the CS-based data-driven bearing fault diagnosis.

## Keywords

Compressive sensing, high-speed train bearings, ASFBP, adaptive thresholds, state assessment

## Introduction

High-speed trains are modern complex mechanical systems, often operating at speeds exceeding 200 km/h. As key components of transmission systems, bearings are susceptible to failures and accidents due to their continuous exposure to reciprocating impacts and harsh environmental conditions.<sup>1</sup> The prevailing regular maintenance approach often leads to excessive maintenance. To address this issue, condition monitoring-based maintenance strategies have emerged, enabling better accident prevention, improved operational safety, and enhanced maintenance cost-effectiveness.<sup>2</sup> Consequently, the health status monitoring and fault diagnosis of high-speed train bearings have attracted extensive attention from the scientific and engineering communities.<sup>3–5</sup>

Among the various techniques available for bearing condition monitoring, acoustic emission (AE) technology stands out for the following advantages<sup>1</sup>: (1)

insensitivity to structural resonance and minimal impact from typical mechanical background noise; (2) high sensitivity to fault activities; (3) capability to fault location.<sup>6</sup> Yoshioka and Fujiwara<sup>7</sup> were the first to

<sup>1</sup>School of Mechanical, Electronic and Control Engineering, Beijing Jiaotong University, Beijing, China

<sup>2</sup>Key Laboratory of Vehicle Advanced Manufacturing, Measuring and Control Technology, Beijing Jiaotong University, Ministry of Education, Beijing, China

<sup>3</sup>School of Mechanical Engineering, Hebei University of Technology, Tianjin, China

<sup>4</sup>Key Laboratory of Advanced Intelligent Protective Equipment Technology, Ministry of Education, Tianjin, China

## Corresponding author:

Hongyuan Qi, School of Mechanical, Electronic and Control Engineering, Beijing Jiaotong University, No.3 Shangyuancun Haidian District, Beijing 100044, China.  
Email: [hyqi@bjtu.edu.cn](mailto:hyqi@bjtu.edu.cn)

apply AE to diagnose bearing faults. Subsequently, Eftekharnejad et al.<sup>8</sup> introduced the spectral kurtosis (SK) method for bearings fault diagnosis, demonstrating AE's heightened sensitivity to early faults. Mahajan and Banerjee<sup>9</sup> identified rail section damage using waveform parameters of AE signals. Additionally, Hou et al.<sup>10</sup> explored AE's applicability in the fault diagnosis of high-speed train bearings and proposed a method for early fault diagnosis under complex conditions. The fault diagnosis technique based on AE has been proved to be a highly effective technique for monitoring the status of high-speed train bearings.<sup>1,4,10</sup> However, high-speed trains encounter multiple sources of interference during operation, including aerodynamic noise, harmonic interference from transmission systems, and random noise.<sup>4</sup> These interferences reduce the signal-to-noise ratio (SNR) of AE signals generated by early damage in high-speed train bearings, present intriguing but challenging aspects in the fault diagnosis of high-speed train bearings.

Traditionally, the Nyquist sampling theorem dictates that the sampling frequency must be at least twice the maximum frequency of the signal. Consequently, the high frequency and broad distribution of the AE signals necessitate high hardware sampling rates (several MHz) for high-speed train bearings condition monitoring systems (CMS). Additionally, as the number of sensors increases under the theory of multisource information fusion,<sup>11</sup> a vast amount of data is generated. As such, conducting front-end rapid diagnosis and compressed data acquisition and reconstruction while operating within limited computing power and transmission bandwidth has emerged as a critical problem for further development of AE-based high-speed train bearing fault diagnosis. Compressed sensing (CS) is a revolutionary and exciting signal processing technique and has been rapidly developed as an important means to break the bottleneck of sampling rate.<sup>12,13</sup> By leveraging sparse a priori knowledge of the signal, CS enables sampling well below the Nyquist frequency and reconstructing the original signal using reconstruction methods. CS has already found applications in diverse fields, such as power systems,<sup>14</sup> wind turbines,<sup>15</sup> earthquakes,<sup>16</sup> and concrete structure,<sup>17</sup> yielding remarkable results. Recently, several studies have introduced CS into bearing fault diagnosis. Liu et al.<sup>18</sup> pioneered the integration of CS into bearings fault diagnosis based on AE, proposing an AE compression feature extraction method for bearing state evaluation in laboratory environments. Furthermore, Bao et al.<sup>19</sup> proposed a CS-based wireless sensor group sparse optimization method for SHM. Banerjee et al.<sup>20</sup> investigated the applicability of CS-based signal recovery technology for ultrasonic SHM where sensors data are prone to loss. While CS theory exhibits great potential and

promising application prospects in mechanical fault diagnosis, its systematic research and application in high-speed train bearings fault diagnosis remain relatively scarce to our knowledge.

The reconstruction recovery process is the basis and core of CS<sup>12,21</sup> and commonly involves two algorithms: greedy algorithms and convex relaxation algorithms. Convex relaxation algorithms are known for their high reconstruction accuracy. However, they become computationally complex when handling signals with lengths exceeding 256.<sup>22</sup> Conversely, greedy algorithms offer advantages such as lower computational cost, simple geometric interpretation, and no limitations regarding complex numbers.<sup>23</sup> Hence, they can be used to reconstruct damage AE signals from high-speed train bearings. Among various greedy matching pursuit (MP) methods, Mallat's representative MP method<sup>24</sup> has paved the way for numerous subsequent variations. MP selects an atom (column of  $\mathbf{D}$ ) from the dictionary matrix  $\mathbf{D}$  that best matches the signal in each iteration, using the selected atom to update the sparse estimate and residuals until a termination rule is met. However, MP can be suboptimal due to the nonorthogonality of the residuals with the selected atoms.<sup>25</sup> To address this limitation, the orthogonal matching pursuit (OMP)<sup>25</sup> introduced a least squares minimization step, ensuring orthogonality between the residuals and selected atoms, thereby enhancing reconstruction accuracy and speed. Since MP and OMP select only one atom per iteration, each reconstruction for a signal with sparsity  $K$  requires  $K$  iterations. To reduce the number of iterations, generalized OMP (gOMP)<sup>26</sup> fixedly selects multiple most relevant atoms in each iteration. Other similar algorithms include regularized OMP (ROMP).<sup>27</sup> Because greedy algorithms are short-sighted by nature,<sup>28</sup> which may lead to incorrect signal estimates, especially with large sparsity  $K$ . The subspace pursuit (SP)<sup>29</sup> and compressive sampling matching pursuit (CoSaMP)<sup>30</sup> methods, employing a two-stage threshold framework, incorporate backtracking in the iterations. Besides, Su et al.<sup>31</sup> proposed an OMP method based on adaptive artificial bee colony algorithm (AABC-OMP). AABC-OMP no longer searches the optimal matching atom, but the optimal parameter.

However, the above methods require prior knowledge of sparsity  $K$  for accurate recovery, which is typically unavailable in practical applications. For this reason, sparsity adaptive matching pursuit (SAMP)<sup>32</sup> was proposed, introducing staging and eliminating the requirement for a priori knowledge of the sparsity  $K$ , but requiring the determination of a fixed stepsize. Subsequently, Wang et al.<sup>33</sup> proposed variable stepsize SAMP, which improves the convergence speed by introducing a variable stepsize correction factor. To further improve the reconstruction accuracy, the

forward-backward pursuit (FBP)<sup>34</sup> was introduced as a new two-stage reconstruction method. It gradually expands the support sets with a fixed stepsize by controlling the step difference between the atomic forward selection stage and the backward deletion stage. FBP can reconstruct the estimated support set with an unknown sparsity  $K$ . Aziz et al.<sup>35</sup> proposed an adaptive iterative forward-backward algorithm (AFB), AFB improves the speed of reconstruction by fixedly selecting and deleting multiple atoms. To overcome the limitation of long reconstruction time of FBP with small stepsize differences, Pan et al.<sup>36</sup> proposed the current latest variable stepsize FBP (VSFBP) method. VSFBP achieves variable stepsize selection and atom deletion by introducing fuzzy thresholds, and updating the observation matrix after each iteration. This innovation addresses the excessive backtracking issue in the backward deletion stage and further improves reconstruction performance. Nevertheless, VSFBP requires presetting the random fuzzy thresholds, and its reconstruction performance is susceptible to the thresholds. Hence, the first type of greedy algorithms, which focus solely on atom forward selection, and the second type, which incorporates backtracking, require prior sparse information about the signal. Although the third type of greedy algorithms does not demand sparsity a prior information and can adjust atom selection and deletion through fixed or variable stepsizes, the matching accuracy is low and requires presetting the stepsize initial conditions. Moreover, the algorithmic performance is sensitive to the initial conditions, limiting the improvement of reconstruction accuracy and speed.

To the best of our knowledge, CS can be effectively applied to fault diagnosis of high-speed train bearings based on AE. Despite the progress in reconstruction method research, the accuracy and speed of reconstruction are still affected and restricted by the prior initial conditions. Additionally, most research has been confined to laboratory environments, with limited application in real industrial sites.

To address these shortcomings, this study presents adaptive dynamic thresholds applicable to adaptive stepsize FBP (ASFBP) and an AE-based bearing state assessment method for high-speed trains. First, the adaptive dynamic thresholds are determined based on the residual feedback mechanism and the atom quality distribution law, realizing adaptive atom selection and deletion and thereby enhancing reconstruction accuracy and speed. Then, the initial dictionary design is improved based on the AE hit characteristics. In terms of bearing health state assessment, a novel evaluation index, the damage state comprehensive evaluation index (DSCEI), is established by combining the compression domain energy parameter with AE time domain hit parameters for the evaluation of bearing

damage states in high-speed trains. Finally, the proposed method's effectiveness and stability are verified under complex conditions that closely resembled actual high-speed train operations.

The main contributions of this article are as follows:

- (1) By employing the residual feedback mechanism and atom quality distribution law, the adaptive dynamic thresholds applicable to ASFBP are proposed to improve the accuracy and speed of reconstruction.
- (2) The DSCEI is established based on AE time-domain hit parameters and compression-domain energy parameter for the quantitative assessment of high-speed train bearing condition.
- (3) The validity and stability of the method are verified under real operating conditions close to high-speed trains, providing a valuable engineering case for the application of CS in data-driven bearing fault diagnosis.

The remainder of this article is organized as follows: “Compressive sensing theory” section analyzes the theoretical basis of CS, as well as the VSFBP method. In “The proposed method” section, the proposed method is presented, followed by simulation analysis of ASFBP. In “Experimental study” section, the method is validated by experimental studies. Finally, “Conclusions” section presents the conclusions.

## Compressive sensing theory

### Theoretical fundamentals

CS comprises two stages: compressed measurement and reconstruction recovery. In the compressed measurement, considering a sparse signal  $\mathbf{x} \in \mathbb{R}^{N \times 1}$ , where  $\mathbb{R}^{N \times 1}$  represents a real column vector with  $N$  elements. The compression process is described as follows.

$$\mathbf{y} = \Phi \mathbf{x} \quad (1)$$

where  $\mathbf{y} \in \mathbb{R}^{M \times 1}$  represents the compressed measurement,  $\Phi \in \mathbb{R}^{M \times N}$  represents the measurement matrix and  $M \leq N$ . Then the compression ratio  $C_r$  is defined as depicted in Equation (2).

$$C_r = M/N \quad (2)$$

If  $\mathbf{x}$  is nonsparse, a sparse representation is necessary to enable compression:

$$\mathbf{x} = \Psi \boldsymbol{\theta} = \sum_{i=1}^N \psi_i \theta_i \quad (3)$$

where  $\Psi \in \mathbb{R}^{N \times N}$  represents a basis or dictionary and the orthogonal basis vectors  $\psi_i$  as the columns, called atoms.

According to Equations (1) and (3), the following equation can be obtained:

$$\mathbf{y} = \Phi \mathbf{x} = \Phi \Psi \boldsymbol{\theta} = \mathbf{A} \boldsymbol{\theta} \quad (4)$$

where  $\mathbf{A} = \Phi \Psi$  is the sensing matrix.

The compressed measurement  $\mathbf{y}$  can be regarded as a linear observation of  $\boldsymbol{\theta}$  through the sensing matrix  $\mathbf{A}$ . The framework of CS is shown in Figure 1. When the compressed measurement contains noise,  $\mathbf{A}$  must satisfy the restrained isometric property (RIP) to ensure successful reconstruction.<sup>12</sup> The Gaussian matrix  $\mathbf{G}$  has been verified to satisfy the RIP, whose elements are independently distributed standard normal random variables that can be generated by random numbers.<sup>21</sup>

In the reconstruction recovery process,  $\boldsymbol{\theta}$  can be reconstructed by solving Equation (5).

$$\hat{\boldsymbol{\theta}} = \arg \min_{\boldsymbol{\theta}} \|\boldsymbol{\theta}\|_0, \quad s.t. \mathbf{y} = \mathbf{A} \boldsymbol{\theta} \quad (5)$$

However, the  $\ell_0$ -norm is an NP-hard problem. To address this problem, numerous studies have transformed the combinatorial optimization problem into a convex optimization problem, seeking equivalent solutions, as depicted in Equation (6):

$$\hat{\boldsymbol{\theta}} = \arg \min_{\boldsymbol{\theta}} \|\boldsymbol{\theta}\|_1, \quad s.t. \mathbf{y} \approx \mathbf{A} \boldsymbol{\theta} \quad (6)$$

Typically, the greedy-type methods (including OMP, ROMP, CoSAMP, FBP, VSFBP, etc.) can efficiently reconstruct a sparse signal  $\hat{\boldsymbol{\theta}}$  and eventually obtain a suboptimal solution. These methods are computationally inexpensive and highly practical.<sup>23</sup>

### VSFBP method

Building upon the FBP method,<sup>34</sup> the two-stage VSFBP<sup>36</sup> method accelerates atom forward selection

and backward deletion steps by incorporating two fuzzy threshold parameters  $\eta_1$  and  $\eta_2$ . Its main steps are as follows:

Step 1. Input parameters and initialization. The observation matrix  $\Phi$  and compressed measurement  $\mathbf{y}$  are inputted.  $\eta_1$  and  $\eta_2$ , where  $\eta_1 = \varepsilon + (1 - \varepsilon) \times \text{rand}(1)$ ,  $\varepsilon \in (0, 1)$  and  $\eta_2 \in (0, 1)$  are set. The maximum number of cycles is denoted by  $k_{\max}$ , and the iteration termination parameter is denoted by  $\varepsilon_0$ . Initial atom support set  $\mathcal{T}^0 = \emptyset$ , current selected atom set  $\mathcal{T}_f = \emptyset$ , current error atom set  $\mathcal{T}_b = \emptyset$ , the initial residual  $r^0 = \mathbf{y}$ , and the iteration initial value  $k = 1$ , where  $\emptyset$  represents a null set.

Step 2. Forward selection stage. An indeterminate number of atoms are selected to determine the support estimate  $\mathcal{T}_f$  based on the  $\eta_1$ ,  $\mathcal{T}_f = \{i | \mu_i \geq \eta_1 \times \max(|\Phi^* r^{k-1}|)\}$ . The observation matrix  $\Phi$  is backed up and updated,  $\{\Phi_\alpha = 0 | \alpha \in \mathcal{T}_f\}$ . Then, the support set is combined,  $\tilde{\mathcal{T}}^k = \mathcal{T}^{k-1} \cup \mathcal{T}_f$ . The least-squares solution<sup>26</sup> is performed based on  $\tilde{\mathcal{T}}^k$ ,  $\mathbf{v} = (\Phi_{\tilde{\mathcal{T}}^k}^T \Phi_{\tilde{\mathcal{T}}^k})^{-1} \Phi_{\tilde{\mathcal{T}}^k}^T \mathbf{y}$ , and the projection coefficients  $\mathbf{v}$  of the reconstructed signal are obtained.

Step 3. Backward deletion stage. An indeterminate number of atoms with smaller projection coefficients are selected based on the  $\eta_2$ ,  $\mathcal{T}_b = \{i | v_i < \eta_2 \times \max(v)\}$ . Then, the current error support set  $\mathcal{T}_b$  is removed from  $\tilde{\mathcal{T}}^k$ ,  $\mathcal{T}^k = \tilde{\mathcal{T}}^k - \mathcal{T}_b$ . Next, the deleted atoms are restored,  $\{\Phi_\beta | \beta \in (\mathcal{T}_f - \mathcal{T}_b)\}$  and  $\mathbf{v}$  are calculated based on the final support set  $\mathcal{T}^k$  of the  $k$ th iteration.

Step 4. Residual update. The residual is updated as  $\mathbf{r}^k = \mathbf{y} - \Phi_{\mathcal{T}^k} \mathbf{v}$ . The current iteration is checked for the termination rule:  $\|\mathbf{r}^k\|_2 \leq \varepsilon_0 \|\mathbf{y}\|_2$ . If the termination rule is not satisfied, iterate from step 2 with  $k = k + 1$ .

However, the random selection of  $\eta_1$  introduces measurable fluctuations, leading to uncertainties in the number of iterations. If  $\eta_1$  is randomly assigned an exceedingly large or small value, the atom selection strategy may be affected while the number of iterations fluctuates substantially. In addition, reconstruction

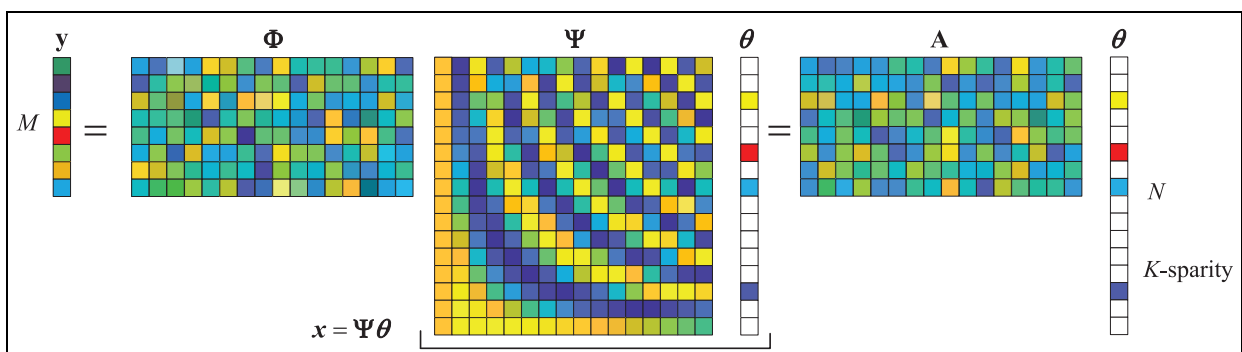


**Figure 1.** The framework of CS. CS: compressed sensing.

performance is affected, and the method's generality and applicability are reduced.

## The proposed method

This section discusses the adaptive dynamic thresholds proposed for atom selection and deletion. In addition, the steps involved in the ASFBP method are detailed. The viability and effectiveness of the adaptive thresholds were verified through simulation analysis. Accordingly, the initial dictionary design was modified. Finally, an overall framework of high-speed train bearing fault diagnosis was established based on CS and AE.

### Adaptive dynamic thresholds

The reconstruction performance of the two-stage reconstruction methods is largely influenced by the threshold values. Therefore, to adaptively select and delete multiple atoms, adaptive dynamic thresholds need to be determined based on the current iteration's reconstruction. The idea of the adaptive dynamic thresholds is as follows: in early iterations, when residuals are large, the atom forward selection threshold and the backward deletion threshold are set to low values, facilitating the selection of more atoms after each iteration. With increasing number of iterations, the residuals gradually decrease. In the later stages of reconstruction, the atoms with the most contribution are selected. The remainder atoms have low relevance and similar qualities. Thus, the atom forward selection threshold and backward deletion threshold should be increased at this point. This reduces the number of atoms to be selected and increases the number of atoms to be deleted, preventing overestimation and oscillations in the late iterations while ensuring satisfactory reconstruction accuracy and speed.

During the forward selection stage, the degree of correlation between the atoms and the current residual is first calculated,  $\mu = |\Phi^* r^{k-1}|$ . Atoms exceeding the adaptive threshold are selected. Based on the above idea, the mean  $\bar{\mu}$  and maximum values of the  $\mu$  are calculated to determine amplitude distribution. Note that the column vectors corresponding to the selected atoms are deleted by setting them to 0.

$$\{\Phi_\alpha = 0 | \alpha \in \mathcal{T}_f\} \quad (7)$$

where  $\mathcal{T}_f$  are the selected atoms.

Consequently, only the nonzero portion of  $\mu$  is considered when calculating  $\bar{\mu}$  as follows.

$$\bar{\mu} = \frac{\sum_{i=1}^N \mu_i (\mu_i \neq 0)}{N - T^{k-1}} \quad (8)$$

where  $T^{k-1}$  represents the total number of atoms removed before  $k$ th iteration.

Furthermore, the centralized distribution degree  $\chi$  of the correlation can be obtained by dividing  $\bar{\mu}$  by the maximum value as in Equation (9).

$$\chi = \bar{\mu} / \max(\mu_i) \quad (9)$$

In addition, given that the current residuals can reflect various stages of reconstruction, it is crucial to consider the fluctuations in residuals during the reconstruction process while determining the adaptive thresholds. The defined residual ratio  $\eta$  is shown in Equation (10):

$$\eta = \frac{\|r^{k-1}\|_2}{\|y\|_2} \quad (10)$$

where  $r^{k-1}$  denotes the residual of the  $k$ th iteration.

As depicted in Equation (10), the residual  $r^{k-1}$  gradually decreases from  $\|y\|_2$  to close to 0 during the reconstruction process, while the compression measurement  $y$  remains fixed, and  $\eta$  decreases from 1 to close to 0. If the  $\eta$  is multiplied and divided directly in this scenario may have a negative impact in the late reconstruction stage and hinder its effectiveness as feedback. To address this, we performed a logarithmic conversion, which altered the variation range of  $\eta$  without affecting its monotonicity. The residual feedback factor  $\eta_{\text{res}}$  is defined as follows:

$$\eta_{\text{res}} = \log(e + 1 - \eta) \quad (11)$$

where  $e$  is the natural constant.

Based on comprehensive consideration of the amplitude distribution of the atom correlation degree and the reconstruction residuals, the adaptive threshold for the forward selection stage is determined as in Equation (12).

$$\gamma_f = \eta_{\text{res}} \times \left\{ 1 - \tau \times \left( 1 - \frac{\left( \frac{1}{N-T^{k-1}} \sum_{i=1}^N |\langle \varphi_i, r^{k-1} \rangle| \right)}{\max(|\langle \varphi_i, r^{k-1} \rangle|)} \right) \right\} \quad (12)$$

where  $k$  is the number of iterations, and  $\tau$  is 0.8.

In the atom backward deletion stage, the estimated projection coefficients of the signal are first calculated based on the least squares method. Then, the atoms with projection coefficients lower than the adaptive threshold are deleted to enhance the reconstruction accuracy. Because the forward selection stage already fully considered the quality of the atoms, the probability of selecting incorrect atoms is minimized. Therefore, in the backward deletion stage, the adaptive threshold

is set to target the median of the atom projection coefficients, and it also incorporates the residual feedback mechanism. This process eliminates atoms with small projection coefficients, further improving the accuracy of atom selection and ensuring efficient reconstruction. The final determined adaptive threshold for the backward deletion stage is as follows:

$$\gamma_b = \frac{1}{2} \times \eta_{\text{res}} \quad (13)$$

The flowchart of adaptive dynamic thresholds is illustrated in Figure 2. The adaptive thresholds not only fully consider the correlation degree between the atoms and the residuals, along with their distributions, but also incorporate the residual feedback mechanism. It enables fast approximation with large steps in the early iterations and accurate approximation with small steps in the late iterations, thereby ensuring reconstruction accuracy and speed.

### ASFBP method

By replacing  $\eta_1$  and  $\eta_2$  in VSFBP<sup>36</sup> with adaptive thresholds, the other reconstruction steps are consistent with the FBP class of the algorithm,<sup>34,35</sup> and ASFBP proceeds as follows:

Step 1. Input parameters and initialization. The observation matrix  $\Phi$ , compressed measurement  $y$ , the maximum number of loops  $k_{\max}$ , and the iteration termination parameter  $\epsilon$  are inputted. Initial atom support set  $T^0 = \emptyset$ , current selected atom set  $T_f = \emptyset$ , current error atom set  $T_b = \emptyset$ , initial number of atom deletions  $T^0 = 0$ , the initial residual  $r^0 = y$ , and the iteration initial value  $k = 1$ , where  $\emptyset$  represents a null set.

Step 2. The inner product  $g_i$  of the atoms  $\varphi_i$  to be selected and the current residual  $r^{k-1}$  are calculated to determine the correlation between them,  $g_i = |\langle \varphi_i, r^{k-1} \rangle|$ . Then, the maximum value  $g_{\max}$  and the average value  $g_{\text{mean}}$  of the correlation coefficients are calculated. Then the residual feedback factor  $\eta_{\text{res}}$  is calculated according to the current residual  $r^{k-1}$ .

$$\begin{cases} g_{\max} = \max(|\langle \varphi_i, r^{k-1} \rangle|) \\ g_{\text{mean}} = \frac{1}{N-T^{k-1}} \sum_{i=1}^N |\langle \varphi_i, r^{k-1} \rangle| \\ \eta = \frac{\|r^{k-1}\|_2}{\|y\|_2} \\ \eta_{\text{res}} = \log(e + 1 - \eta) \end{cases} \quad (14)$$

Step 3. The adaptive threshold  $\gamma_f = \eta_{\text{res}} \{1 - \tau \times (1 - g_{\text{mean}}/g_{\max})\}$  is calculated with a maximum limited to 1, and the atoms  $T_f = \{i | g_i \geq \gamma_f \times g_{\max}\}$  that satisfies the condition in the atom forward selection stage are selected. Then the atom support set is combined,  $\tilde{T}^k = T^{k-1} \cup T_f$ . The observation matrix  $\Phi$  is backup, and the observation matrix is updated,  $\{\Phi_\xi = 0 | \xi \in T_f\}$ .

Step 4. The least squares solution is performed based on the current support set  $\tilde{T}^k$ , and the projection coefficients  $\hat{\theta}$  of the reconstructed signal are obtained.

$$\hat{\theta} = \arg \min_{\hat{\theta}} \|y - \Phi_{\tilde{T}^k} \hat{\theta}\|_2 = (\Phi_{\tilde{T}^k}^T \Phi_{\tilde{T}^k})^{-1} \Phi_{\tilde{T}^k}^T y \quad (15)$$

Step 5. The adaptive threshold  $\gamma_b$  for the atom backward deletion stage is calculated based on the residual feedback factor  $\eta_{\text{res}}$ , and the atoms with smaller projection coefficients form the set  $T_b = \{i | \hat{\theta}_i < \gamma_b \times \max(|\hat{\theta}|)\}$ . Then the current error support set  $T_b$  is removed from the atom support set

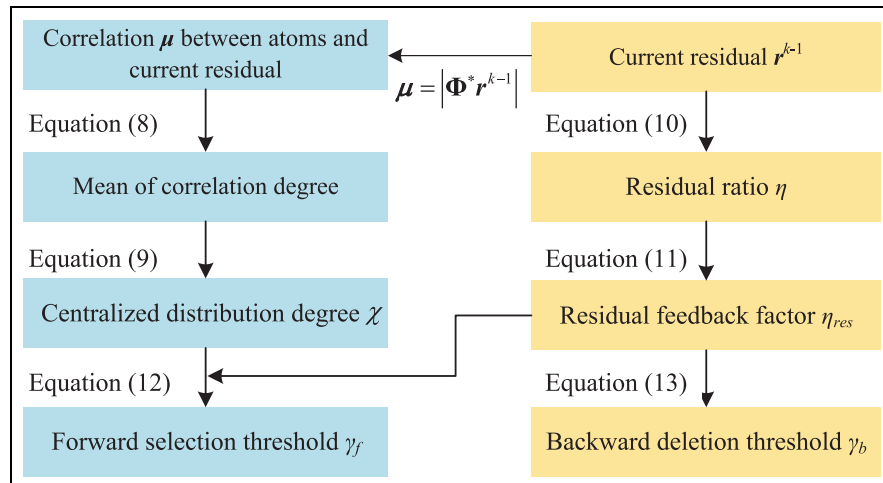


**Figure 2.** Flowchart of the adaptive dynamic thresholds.

$\tilde{\mathcal{T}}^k$ ,  $\mathcal{T}^k = \tilde{\mathcal{T}}^k - \mathcal{T}_b$ . Additionally, the length of  $\mathcal{T}^k$  is calculated as  $T^k$ .

Step 6. The partially deleted atoms  $\{\Phi_\zeta | \zeta \in (\mathcal{T}_f - \mathcal{T}_b)\}$  are recovered. Then, the least squares solution is performed again based on the final support set  $\mathcal{T}^k$  of the current iteration to obtain the new projection coefficients  $\hat{\boldsymbol{\theta}}$ .

$$\hat{\boldsymbol{\theta}} = \arg \min_{\hat{\boldsymbol{\theta}}} \|\mathbf{y} - \Phi_{\mathcal{T}^k} \hat{\boldsymbol{\theta}}\|_2 \quad (16)$$

Step 7. The residual  $\mathbf{r}^k$  is updated as  $\mathbf{r}^k = \mathbf{y} - \Phi_{\mathcal{T}^k} \hat{\boldsymbol{\theta}}$  based on the final projection coefficients  $\hat{\boldsymbol{\theta}}$ .

Step 8. The result of the current iteration is checked for the termination rule:  $\|\mathbf{r}^k\|_2 \leq \varepsilon \|\mathbf{y}\|_2$  or  $|T^k| \geq M$ . If it does not satisfy the rule, the iteration is repeated from Step 2 with  $k = k + 1$ .

### Simulation analysis and verification

First, the feasibility of adaptive dynamic thresholds and the accuracy of ASFBP are preliminarily verified based on simulated signals and compared with other typical MP type algorithms. The simulated data not only provide a basis for theoretical analysis and algorithm design, but can also be used to study the performance of ASFBP under given parameters (sparsity and SNR). The simulated signal is a sparse signal of length 256, wherein the nonzero atoms obey a Gaussian distribution, the sparse basis is a unit diagonal matrix, and the measurement matrix is Gaussian matrix  $\mathbf{G}$  (size  $128 \times 256$ ). The simulation was performed on a laptop with an Intel® CoreTM i7-10510 CPU@1.8 GHz and 12.0 GB RAM using MATLAB R2021A. The parameters of the VSFBP<sup>36</sup> were set as  $\eta_1 = 0.4 + 0.6 \times \text{rand}(1)$ , and  $\eta_2 = 0.8$ . The parameters of the FBP<sup>34</sup> were set to  $\alpha \in [0.2M, 0.3M]$  and  $\alpha - \beta = 1$ , where  $M$  denotes the number of rows in the

measurement matrix, and  $\alpha$  and  $\beta$  are the number of atoms selected and deleted in per iteration, respectively. All these values are based on the prior literature on reconstruction methods.<sup>34,36</sup> The number of atoms per selection of gOMP<sup>26</sup> was set to  $K/4$ , where  $K$  is the sparsity. The iteration termination parameter  $\varepsilon_0$  was set to  $10^{-6}$ , and the maximum number of loops was  $M$  for the algorithms. The simulations were run 500 times, and the reconstruction accuracy and speed of the methods were analyzed from three aspects: exact reconstruction rate, average normalized mean-squared-error (ANMSE), and running time. The condition for signal exact reconstruction is  $\|\mathbf{x}_i - \hat{\mathbf{x}}_i\|_2 \leq 10^{-6}$ , so the exact reconstruction rate can be obtained by dividing the number of successful reconstructions by 500. The ANMSE and relative error (RE) are defined as follows:

$$\text{ANMSE} = \frac{1}{N_{um}} \sum_{i=1}^{N_{um}} \frac{\|\mathbf{x}_i - \hat{\mathbf{x}}_i\|_2^2}{\|\mathbf{x}_i\|_2^2} \quad (17)$$

$$\text{RE} = \frac{\|\mathbf{x} - \hat{\mathbf{x}}\|_2}{\|\mathbf{x}\|_2} \quad (18)$$

where  $N_{um}$  is the number of runs,  $\mathbf{x}_i$  and  $\mathbf{x}$  are the original signals, and  $\hat{\mathbf{x}}_i$  and  $\hat{\mathbf{x}}$  are the reconstructed signals.

The simulation results are illustrated in Figure 3. In terms of exact reconstruction rate and ANMSE, the ASFBP, the VSFBP, and the FBP, all having a back-tracking process, demonstrate higher exact reconstruction rates and lower ANMSE. Conversely, the results obtained by the OMP and the gOMP show higher error and lower exact reconstruction rates, with OMP exhibiting the largest error and the lowest exact reconstruction rate. The running time is illustrated in Figure 3(c), where the FBP has the longest running time. Although the gOMP has the fastest running speed, its reconstruction error is relatively large, and its overall

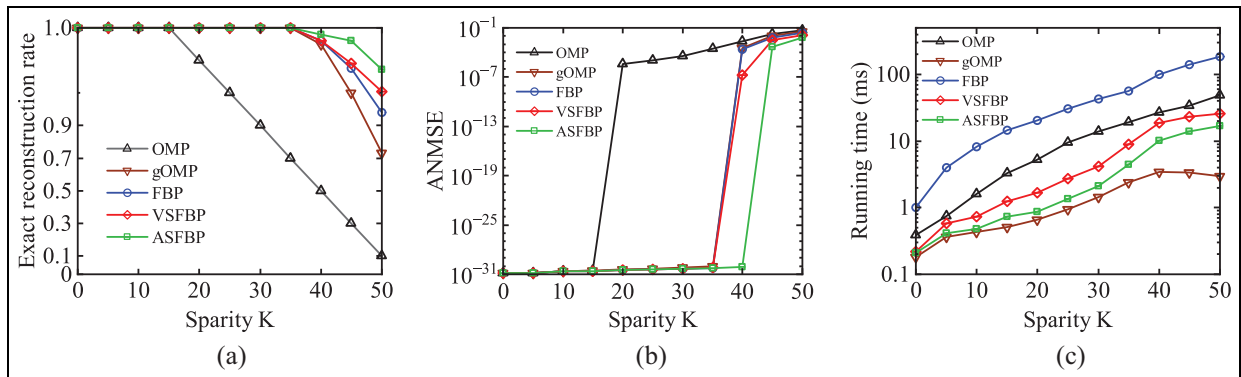


**Figure 3.** Comparison of reconstruction results of different methods: (a) exact reconstruction rate, (b) ANMSE, and (c) running time.

performance only outperforms the OMP among the above methods. The ASFBP shows a shorter running time and faster speed compared to the VSFBP and the FBP. Additionally, for smaller sparsity  $K$ , the reconstruction accuracy is higher, and the running time is shorter. The comprehensive analysis indicates that the ASFBP not only has the highest exact reconstruction rate and the smallest ANMSE but also has a shorter running time than the VSFBP and FBP methods, making it advantageous in terms of reconstruction accuracy and speed.

To further verify the effectiveness of the adaptive dynamic thresholds and compare ASFBP with other advanced two-stage reconstruction methods, the simulated AE signals of high-speed train bearings are as follows:

$$\left\{ \begin{array}{l} x(t) = \sum_{i=1}^{M_0} A_i s_i(t - iT_\alpha) + \sum_{j=1}^{M_1} B_j \sin(2\pi f_j t + \beta_j) \\ + \sum_{k=1}^{M_2} C_k s_k(t - T_k) + n(t) \\ s_i(t) = e^{-2\pi f_i \alpha_0 t} \cos(2\pi f_i t + \varphi_i) \end{array} \right. \quad (19)$$

The first part  $\sum_{i=1}^{M_0} (\cdot)$  represents the impact component of the bearing damage,  $A$  denotes the impact amplitude,  $s_i(t)$  represents the impact response,  $T_\alpha$  denotes the time interval between adjacent faults,  $\alpha_0$  denotes the damping coefficient,  $f_i$  represents the impact frequency, and  $\varphi_i$  is the initial phase. The second part  $\sum_{j=1}^{M_1} (\cdot)$  represents the periodic harmonic interference from the equipment of high-speed trains,  $B$  denotes the amplitude,  $f_j$  represents the impact frequency, and  $\beta_j$  represents the initial phase. The third part  $\sum_{k=1}^{M_2} (\cdot)$  represents the random impulses produced by component collisions or other random shock disturbances during the test.  $C_k$  and  $T_k$  represent the amplitude of the random impulses and their corresponding occurred time, respectively. The fourth part  $n(t)$  is a random white noise used to simulate the background noise with a SNR of 15 dB. The parameters of the simulated signal are provided in Table 1. Figure 4 illustrates the individual components of the simulated signal and displays the time and frequency domains of the mixed signal. The mixed signal contains a high-frequency component of 20 kHz.

The analysis is then performed based on the simulated signal. The atom correlations and thresholds of the ASFBP and VSFBP reconstructions are illustrated in Figure 5. For the VSFBP, although  $\eta_1$  and  $\eta_2$  are fixed during the iterations, the maximum correlation value changes dynamically, which makes the forward selection and backward deletion thresholds unfixed, enabling the dynamic selection and deletion of atoms. However, there are still atoms with large correlation that are not selected in the first eight iterations as can be seen from the correlation maximum. Further combined with the number of correlations of 0 (the selected atoms) demonstrates a slow reconstruction speed. In contrast, the ASFBP has a faster reconstruction speed, which is due to the dynamic changes of the adaptive thresholds  $\gamma_f$  and  $\gamma_b$ . At the early stage of the iterations,  $\gamma_f$  and  $\gamma_b$  are small. The atoms that account for major contribution are rapidly selected at this time, while the correlation decreases rapidly. With the increasing number of iterations, it can be recognized from the correlation distribution that the qualities of atoms are not only at a low level but also closer to each other. In this case,  $\gamma_f$  and  $\gamma_b$  gradually increase and level off, reducing the number of atom selections and improving the correct rate of selection, which ensures high precision and rapidity of the reconstruction. The aforementioned comparison suggests the correctness and rationality of the adaptive dynamic thresholds.

Based on the simulation signal, 100 reconstructions were performed, where a random segment of the signal with a length of 2000 was intercepted each time for reconstruction. The compression ratio  $C_r$  was set to 0.75, using the Fourier dictionary as the sparse basis, and the measurement matrix was Gaussian matrix  $G$ . The results of the RE are illustrated in Figure 6(a). Both ASFBP and VSFBP exhibited similar overall fluctuation changes in the RE, with the ASFBP having an average RE of 47%, which was lower than the 49% of the VSFBP. Additionally, the RE of a single reconstruction exhibited clear differentiation, with most of the RE values being less than 0.8 and a few RE values being greater than 1 because when randomly intercepting a signal segment of length 2000, the intercepted portions contain only the Gaussian white noise portion in  $x(t)$ , which do not contain the impact component of

**Table I.** Parameters of the simulated AE signal.

Fault impact parameters	Value	Harmonic	Value	Random impact	Value
$A$	1 mV	$B_1/B_2$	0.105	$C_1$	2
$T_\alpha$	1/45 s	$f_1$	7 Hz	$C_2$	3
$f$	20 kHz	$f_2$	14 Hz	$C_3$	2.8
$\alpha_0$	0.035	$\beta_1$	$\pi/6$	$M_2$	3
$\varphi$	0	$\beta_2$	$-\pi/3$	$f$	5.4 kHz

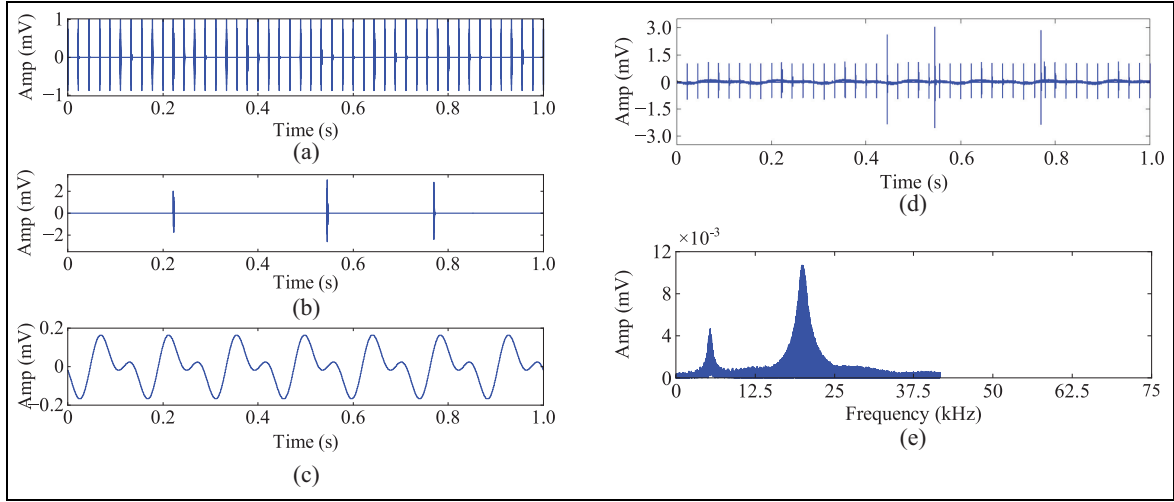


**Figure 4.** Bearing damage AE simulation signal: (a) fault impact signal, (b) random impulses, (c) periodic harmonic signal, (d) mixed signal, and (e) spectrum of mixed signal. AE: acoustic emission.

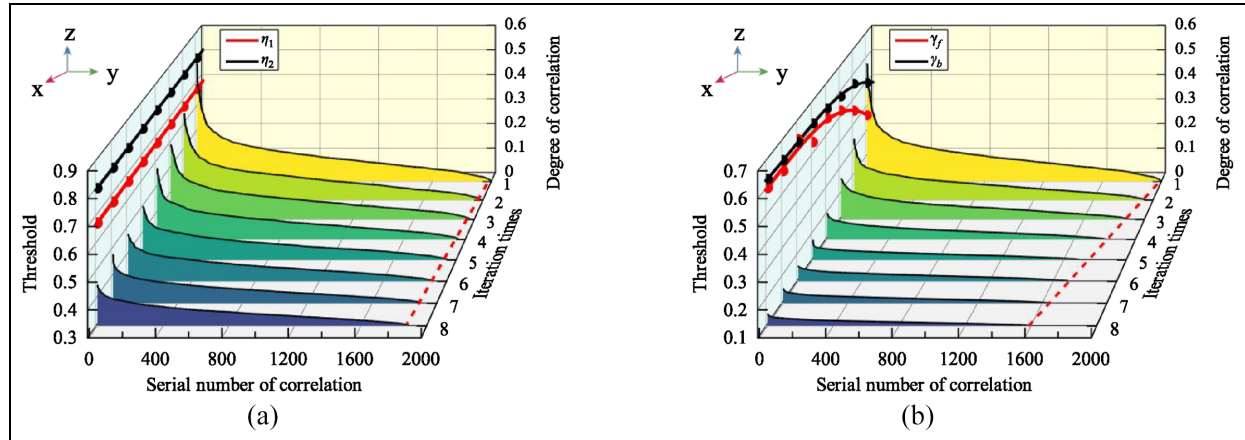


**Figure 5.** Comparison of reconstruction process and thresholds: (a) VSFBP and (b) ASFBP. VSFBP: variable stepsize forward–backward pursuit; ASFBP: adaptive stepsize forward–backward pursuit.

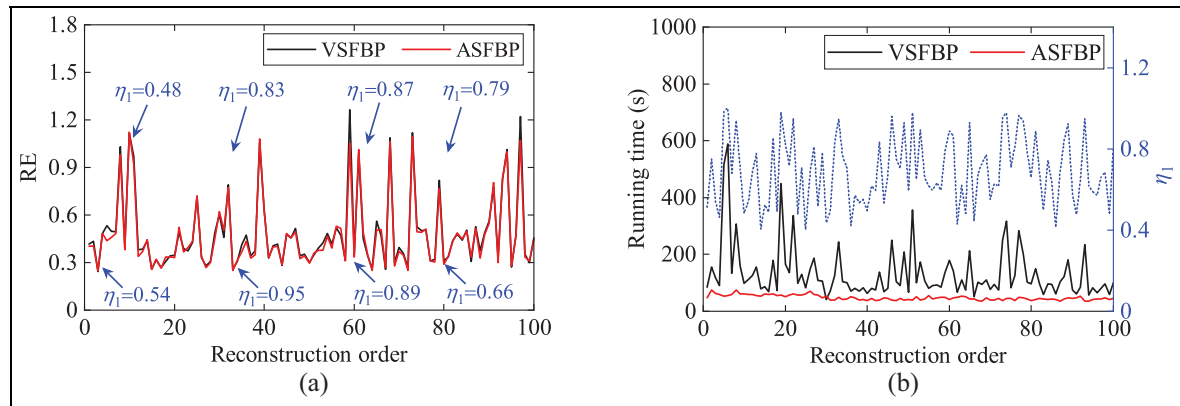


**Figure 6.** Comparison of the reconstruction performance of the ASFBP and VSFBP: (a) RE and (b) running time. VSFBP: variable stepsize forward–backward pursuit; ASFBP: adaptive stepsize forward–backward pursuit; RE: relative error.

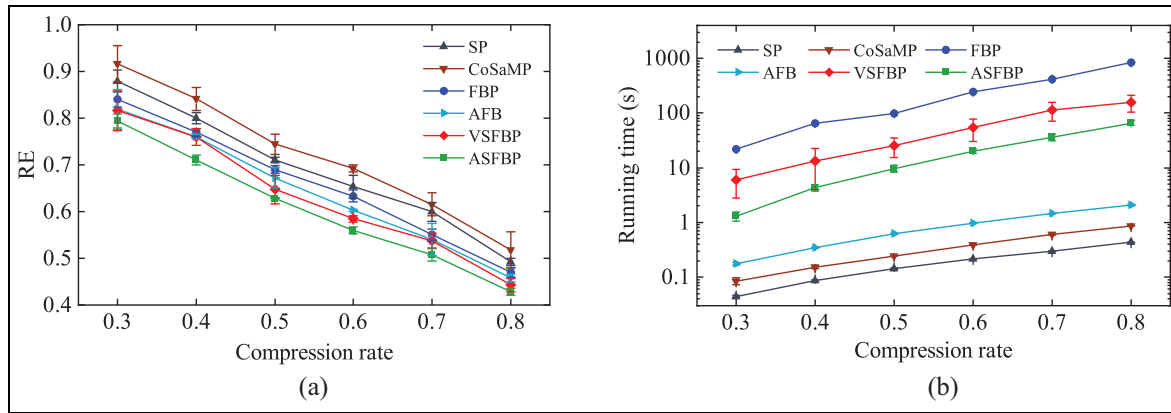


**Figure 7.** Comparison of reconstruction results of simulated AE signal: (a) RE and (b) running time. AE: acoustic emission; RE: relative error.

bearing damage. Because Gaussian white noise cannot be sparsely represented in any transform domain,<sup>37</sup> it caused a large RE. Further analysis of VSFBP revealed that its forward selection threshold  $\eta_1$  was randomly generated, but the existence of the backtracking stage made its RE insensitive to  $\eta_1$ . In terms of reconstruction speed, the fluctuation of the running speed of VSFBP was large. Furthermore, upon combining with the curve of  $\eta_1$ , the curve exhibited consistent fluctuation with the running time curve of VSFBP, the stepsize of the forward selection of atoms becomes larger at this point when the value of  $\eta_1$  was small, and the running time of VSFBP was short with a fixed backward deletion threshold. By contrast, the running time becomes longer when  $\eta_1$  was larger. Thus, the running speed of VSFBP was sensitive to the value of  $\eta_1$ . However, ASFBP maintained a consistently high speed in all 100 reconstructions, and the average running time of the ASFBP method was 48 s, which was considerably much lower than 133 s of VSFBP. The comparison not only revealed the superior performance of ASFBP but also confirmed the correctness and stability of the adaptive dynamic thresholds.

ASFBP is compared with other methods including SP,<sup>29</sup> CoSaMP,<sup>30</sup> FBP,<sup>34</sup> AFB,<sup>35</sup> and VSFBP<sup>36</sup> with typical backtracking steps using simulated signals. The RE and running time of the reconstructions using the methods are depicted in Figure 7. The RE decreases with the increasing value of compression ratio  $C_r$ . Because the larger the value of  $C_r$ , the more information of the original signal is retained in the compressed measurement (when  $C_r$  is 1, the number of compressed measurements is the same as that of the original signal), resulting in a smaller RE. Among these methods, CaSaMP and SP demonstrate higher RE at each given  $C_r$ . VSFBP and AFB, as improved versions of FBP, both demonstrate lower RE than FBP. By contrast,

ASFBP demonstrates the lowest RE. In terms of running time, the running time increases with increasing  $C_r$ , with FBP exhibiting the longest running time and SP exhibiting the shortest running time. The running time of ASFBP is substantially lower than that of FBP and VSFBP. Note that the running time of VSFBP fluctuates considerably because of the use of random numbers for atom selection thresholds.

### Initial dictionary design for AE signal

The aforementioned studies demonstrated that using a fixed dictionary can achieve desirable reconstruction results at low compression rates (larger values of  $C_r$ ). However, at high compression rates, the reconstructed signal often exhibits significant errors. This is mainly because the fixed dictionary may not be able to adequately capture the complex intrinsic structure of real signals, leading to the signal not being sparse enough under the fixed dictionary. In this case, high compression rates violate the number of compressed measurements required for accurate reconstruction.<sup>38</sup> The K-means singular value decomposition (K-SVD)<sup>39</sup> dictionary learning algorithm that enables the construction of a learning dictionary to improve the reconstruction. In the K-SVD, a suitable initial dictionary is essential not only for improving convergence speed and avoiding local optimality but also for enhancing the accuracy of feature learning. An overlapping segmentation strategy was introduced to construct a suitable initial dictionary,<sup>40</sup> which could consider the self-similarity and time-shift invariance of AE signals.

The window length  $L$  and overlap rate  $\delta$  directly affect the correctness and feasibility of the initial dictionary design. A larger  $\delta$  can utilize the self-similarity of AE signals more comprehensively and prevent the loss of useful information.<sup>40</sup>  $L$  determines the effective

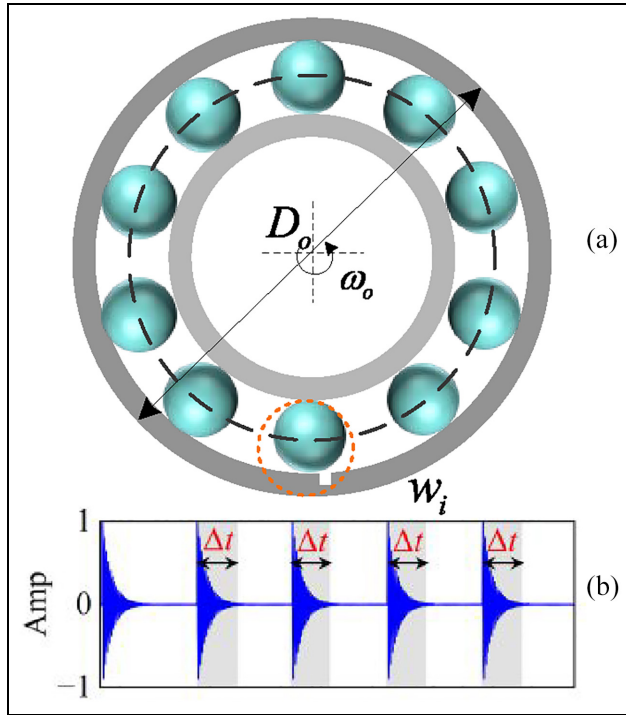


**Figure 8.** AE hit duration estimation model. AE: acoustic emission.

information contained in a single atom. Periodic high-frequency impact on AE signal is generated between rollers entering and exiting a defect when a bearing rotates, as shown in Figure 8. The  $L$  should be no less than the length of a single hit to ensure an accurate representation of bearing damage on the AE features. Moreover, the  $L$  is desirable to be as small as possible to reduce the computational burden. Therefore, an AE hit time parameter model is established to determine a reasonable  $L$ . Figure 8 demonstrates that different defect widths and rotation speeds determine the time for a roller passing through the defect, that is, the duration  $\Delta t$  of a single AE hit. The time  $\Delta t$  is calculated as follows:

$$\Delta t = w_i / v_{or} \quad (20)$$

where  $w_i$  is the width of defects for different damage stages and  $v_{or}$  is the relative speed of the roller to the outer ring. According to the kinematic relationship,  $v_{or}$  is as follows:

$$v_{or} = \pi D_o f_c \quad (21)$$

where  $D_o$  is the diameter of the bearing outer ring and  $f_c$  is the rotation frequency of the cage.

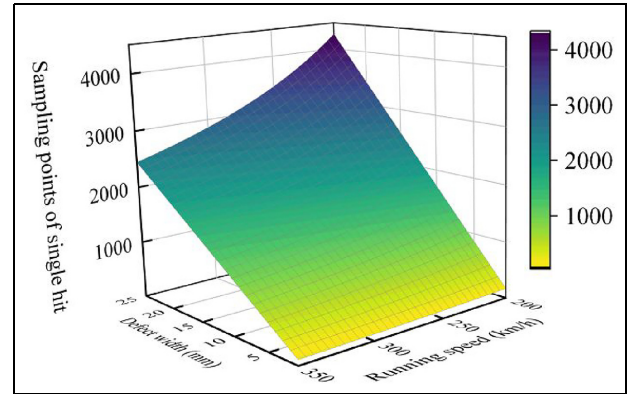


**Figure 9.** Numerical calculations of single hit sampling points.

Based on Equations (20) and (21), given that  $\Delta t = N_0 / f_s$  and  $f_c$ , Equation (22) can be obtained:

$$N_0 = \frac{f_s w_i}{\pi D_o f_c} = \frac{2 f_s w_i D_p}{\pi D_o f_c (D_p - D_b \cos \alpha)} \quad (22)$$

where  $N_0$  is the number of sampling points,  $L \geq N_0$ ,  $f_s$  is sampling frequency,  $D_b$  is roller diameter,  $D_p$  is the bearing pitch diameter,  $\alpha$  is the contact angle, and  $f_o$  is the rotation frequency of the inner ring and rotating shaft.

Figure 9 illustrates the relationship between the number of sampling points of a single hit and running speed and defect width in an ideal environment when  $f_s = 1\text{MHz}$  in Equation (22). The number of sampling points decreases with the increase of running speed and the decrease of defect width. Note that during actual operation of the train, the existence of noise suppresses the lower part of the amplitude, reducing the effective data length of the hits in the waveform stream. Therefore, under real operation conditions, the sampling frequency, running speed, and defects must be considered to determine a reasonable  $L$ .

## Overall framework

The proposed framework for high-speed train bearing fault diagnosis based on CS and AE is illustrated in Figure 10.

## Experimental study

This section discusses an experimental study that was conducted to validate the effectiveness of the adaptive dynamic thresholds and bearing health state assessment method of high-speed trains in a real and complex environment. Then the DSCEI was constructed

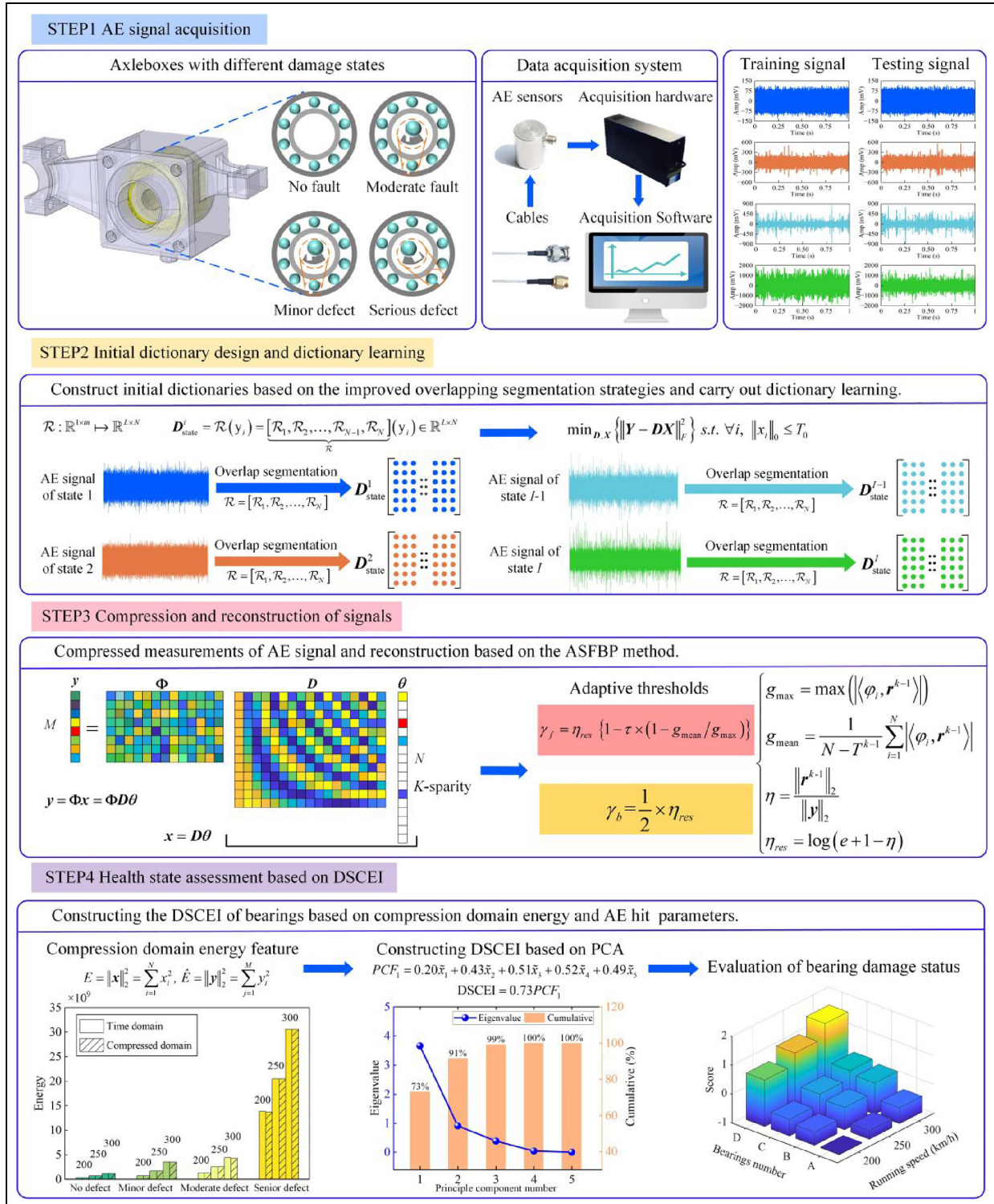


**Figure 10.** Flow of the proposed method.

**Table 2.** AE hardware acquisition parameters settings.

Parameters	Threshold	Sampling frequency	Sampling time	AE timing parameters			Analog filter	Output voltage
				PDT	HDT	HLT		
Value	45 dB	1 MHz	1 s	300 us	600 us	1000 us	50–400 kHz	AC ±2 V

PDT: peak definition time; HDT: hit definition time; and HLT: hit lockout time.

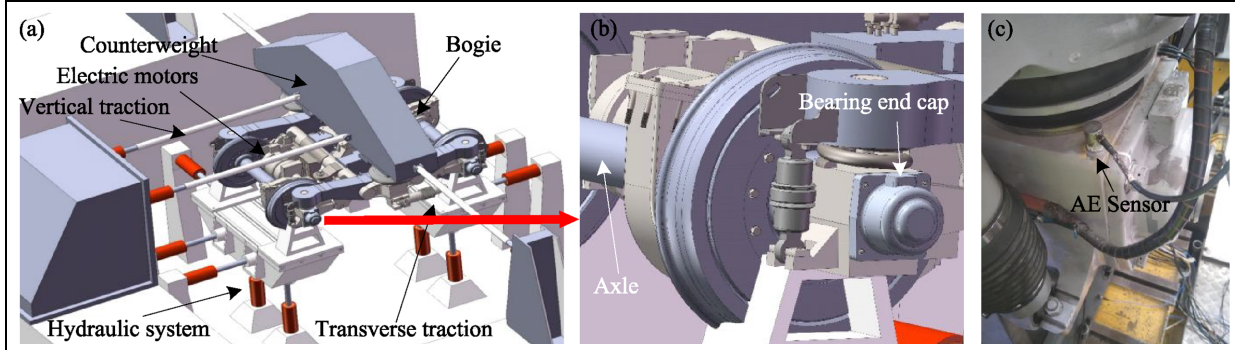


**Figure 11.** Testing device: (a) high-speed train rolling test rig, (b) test rig localization, and (c) sensor installation position.

on this basis to realize the comprehensive evaluation of bearing damage state.

### Experimental test rig

To emulate the operation environment of high-speed trains, a special electric multiple unit test platform was designed and constructed in China National Engineering Laboratory for High-Speed Train. The schematic of the test device is shown in Figure 11. The test rig can accommodate a full-size bogie, consisting of two axles and four sets of bearings. The test platform includes longitudinal traction system, transverse traction system, longitudinal traction system, hydraulic system, electric motors, and other components. The counterweight ensures that each bearing group can bear a load of approximately 5380 kg, thus preventing the bogie from bouncing up and down, and the transverse and longitudinal traction systems help the bogie maintain its position during the wheelset rotation. The hydraulic system applies the road spectrum impact collected on the actual running line for high-speed trains, thereby making the test similar to the actual running environment. The wheels are driven by electric motor at a maximum linear velocity of 350 km/h. During data acquisition, an AE sensor was installed on the upper surface of the axle box near the bearing, and the lower surface of the sensor is applied with an appropriate amount of coupling agent to promote the propagation of the elastic wave. The AE sensor model, PK15I, has a resonant frequency of 150 kHz, ensuring the

high-frequency characteristics of the collected signal. The gain of the built-in circuit of the AE sensor is 26 dB. The acquisition parameters settings are listed in Table 2.

Most of the bearings used in the tests were dismantled from high-speed trains with varying degrees of natural defects in the outer rings. Four categories of bearings were considered: bearing A with no defects, bearing B with minor defects, bearing C with moderate defects, and bearing D with serious defects. Representative bearings from each category were specially chosen for the experiment. Figure 12 illustrates the actual damage states of the four different bearings. The theoretical fault characteristic frequencies of the bearings at running speeds of 200, 250, and 300 km/h were calculated to be 168.15, 210.19, and 252.23 Hz, respectively.

### Experimental verification

The AE signal collected from bearing B at a speed of 300 km/h was used in this study to compare the reconstruction performance of ASFBP and VSFBP in real operating environments. One hundred reconstructions were performed, each time randomly intercepting the AE signal of length 4000, with a  $C_r$  of 0.6. The comparison of RE and running time is illustrated in Figure 13. The RE of the ASFBP and VSFBP is quite similar in overall fluctuation change in terms of reconstruction error, with the average RE of the ASFBP being 33%, which is lower than the 35% of VSFBP. In terms of

reconstruction speed, the running speed of VSFBP fluctuates more widely, and it remains sensitive to  $\eta_1$ . While the running speed of the ASFBP remains consistently fast and smooth, with an average running time of 67 s, significantly shorter than the 224 s of VSFBP. The comparative analysis further validates the effectiveness of adaptive dynamic thresholds and ASFBP in real operating environments.

In order to conduct a more detailed comparison and analysis of the reconstruction process between the ASFBP and the VSFBP, a single hit of the AE signal is reconstructed, while keeping  $C_r$  unchanged. The reconstruction results and their residuals are shown in Figure 14(a). First, a single hit can be fully captured with 4000 data points, confirming the correctness of the AE hit time parameter model. Both methods successfully reconstructed the hit, but the RE of the VSFBP-based reconstructed signal is 38% when  $\eta_1 = 0.67$ , while the RE of the ASFBP-based reconstructed signal is lower at 34%. This indicates that the ASFBP achieves better reconstruction accuracy for a single hit. To analyze the iterative process of both methods, the descending curve

of the residual ratio  $\eta$  is plotted in Figure 14(b) based on Equation (10). In the early stage of iteration,  $\eta$  of the VSFBP declines rapidly, but its decline rate gradually decreases with the increase in the number of iterations. In the late stage of iteration, the decline rate of  $\eta$  keeps at a very low level, which leads to the VSFBP to require more iteration steps to reach the termination rule, with a total of 116 steps. On the other hand, for the ASFBP, in the early stage of iteration,  $\eta$  decreases sharply, and with the increase in the number of iterations, the rate of decrease in  $\eta$  gradually slows down. In the late stage of iteration, although the decrease rate of  $\eta$  decreases, the ASFBP can quickly reach the iteration termination rule with only 39 steps in total. Hence, adaptive dynamic thresholds enable ASFBP to perform fast approximations with large stepsizes in the initial iterations and accurate approximations with small steps in latter iterations. In comparison, the ASFBP is more greedy than the VSFBP.

Figure 15 illustrates a comparison performed using the AE signal of bearing B at a speed of 300 km/h. The length of the intercepted AE signal in the

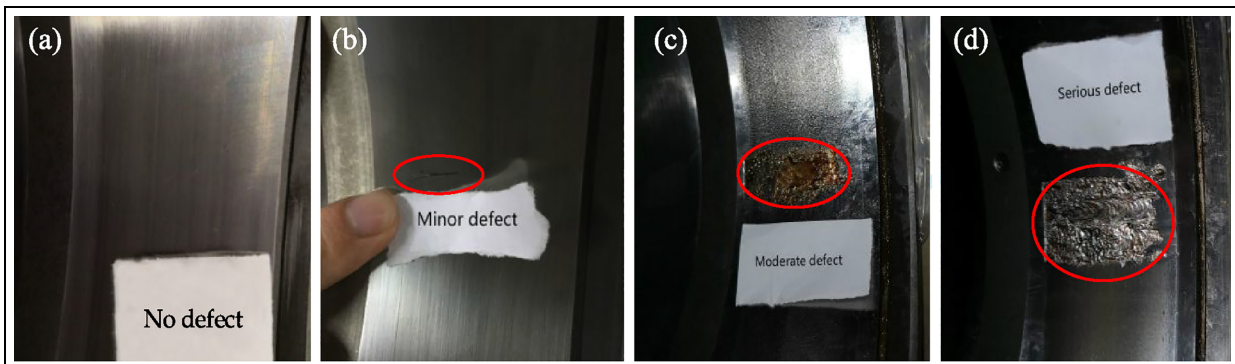


**Figure 12.** Bearings with different degrees of damage: (a) bearing A, (b) bearing B, (c) bearing C, and (d) bearing D.

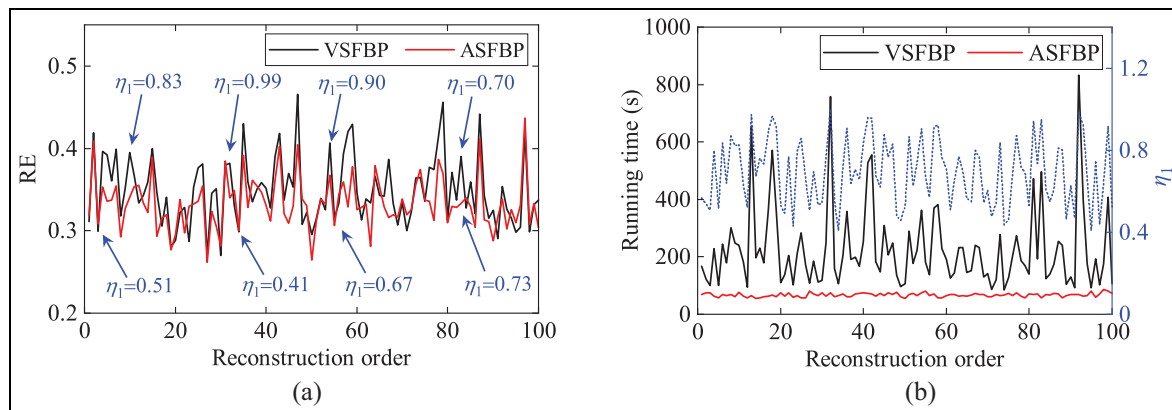


**Figure 13.** Comparison of the reconstruction performance of the ASFBP and VSFBP: (a) RE and (b) running time. VSFBP: variable stepsize forward-backward pursuit; ASFBP: adaptive stepsize forward-backward pursuit; RE: relative error.

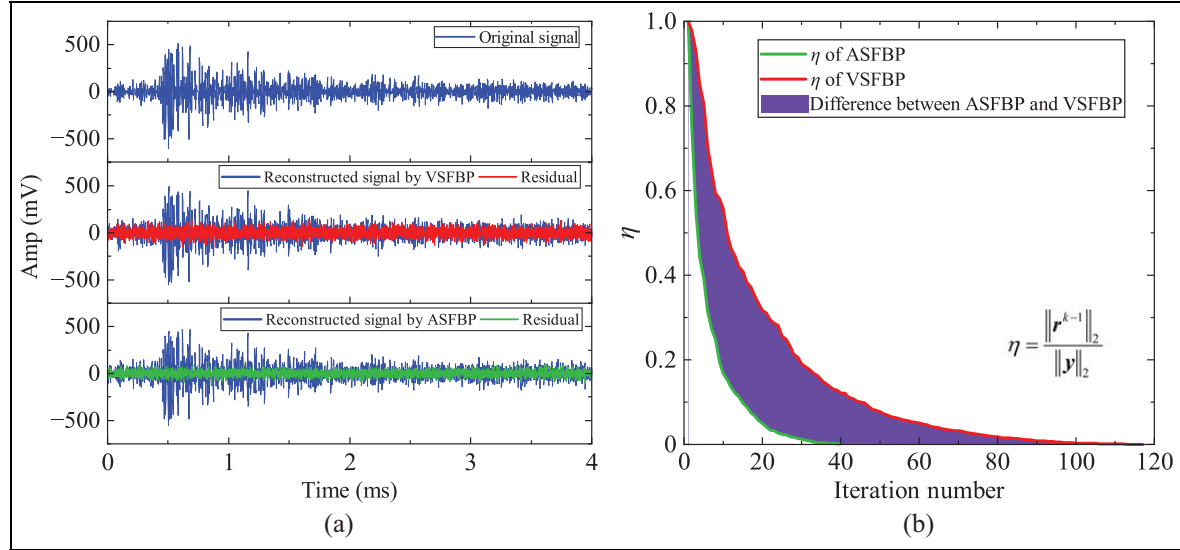


**Figure 14.** Comparison of single-hit reconstruction results and residual ratio  $\eta$ : (a) reconstruction results and (b)  $\eta$ .

reconstruction is 4000. The results are consistent with the simulation results (Figure 7), such that the RE decreases and the running time increases with increasing  $C_r$ . SP and CoSaMP demonstrate shorter running times, but their RE values are higher. By contrast, FBP, AFB, VSFBP, and ASFBP demonstrate lower RE and relatively longer running times. Among them, ASFBP exhibits a higher running speed than VSFBP and FBP while exhibiting the lowest RE. The results for  $C_r$  of 0.6 are depicted in Figure 16. The reconstruction accuracy and speed of ASFBP are overall improved by 10% and three times, respectively, compared with the VSFBP. In terms of reconstruction speed, the coefficient of variation of ASFBP is 5.3%, which is smaller than that of VSFBP (36.6%), indicating that ASFBP provides more stable reconstruction speeds.

The reconstructions of AE signals from bearings with different damage levels are analyzed to verify the effectiveness and robustness of the complete method. First, the overlapping segmentation strategy parameters are determined through the AE hit time parameter model, where the  $L$  is 4000, and the  $\delta$  is 98%. The reconstruction results at 200 km/h speed when  $C_r = 0.05$  are shown in Figure 17. Under high compression ratio, both in the time and frequency domains, as well as in the square of the envelope spectrum, the reconstructed signals adequately retain critical information for fault diagnosis, and they also have smaller reconstruction errors. Among the bearings A, B, C, and D, the reconstruction errors are 67, 47, 49, and 54%, respectively. For bearing A, the acquired signal mainly consists of noise with relatively poor sparsity,

leading to a relatively large RE. For defective bearings, the AE signals have obvious impact characteristics, resulting in better sparsity and lower reconstruction errors. Besides, with the deepening of the damage, the background noise level of the AE signal gradually increases,<sup>4</sup> so the RE shows a certain upward trend. Furthermore, the average time for single-hit reconstruction is only 0.14 s. This is significantly smaller than the average time required using a fixed dictionary, highlighting the effectiveness of the learned dictionaries.

#### Damage state comprehensive evaluation index

The primary objective of a CMS is to rapidly and accurately detect the status of structures. Transmitting raw high-frequency AE signals and extracting fault features from them can be time consuming. Extracting fault features based on the compression domain proves to be an effective method for characterizing the bearing state. According to Equation (1), the restricted isometry of the AE signal  $\mathbf{x} \in \mathbb{R}^{N \times 1}$  can be described as follows:

$$(1 - \delta_K) \|\mathbf{x}\|_2^2 \leq \|\mathbf{y}\|_2^2 \leq (1 + \delta_K) \|\mathbf{x}\|_2^2 \quad (23)$$

The  $\ell_2$ -norm of the AE signal can characterize its energy. Therefore, Equation (23) can be described as the approximate constant energy of the signal before and after compression. Accordingly, the time domain energy  $E$  and the compression domain energy  $\hat{E}$  can be obtained as follows:

$$E = \|\mathbf{x}\|_2^2 = \sum_{i=1}^N x_i^2, \hat{E} = \|\mathbf{y}\|_2^2 = \sum_{j=1}^M y_j^2 \quad (24)$$

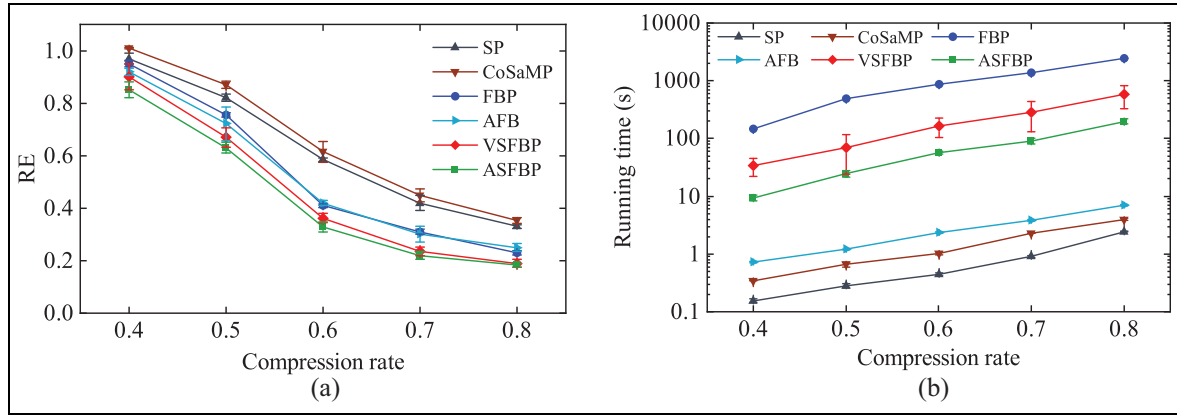


**Figure 15.** Comparison of reconstruction results of test AE signals: (a) RE and (b) running time. AE: acoustic emission; RE: relative error.

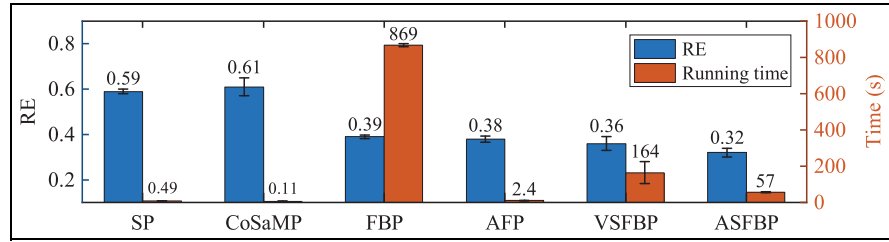


**Figure 16.** Statistics of the reconstruction results at a compression rate of 0.6.

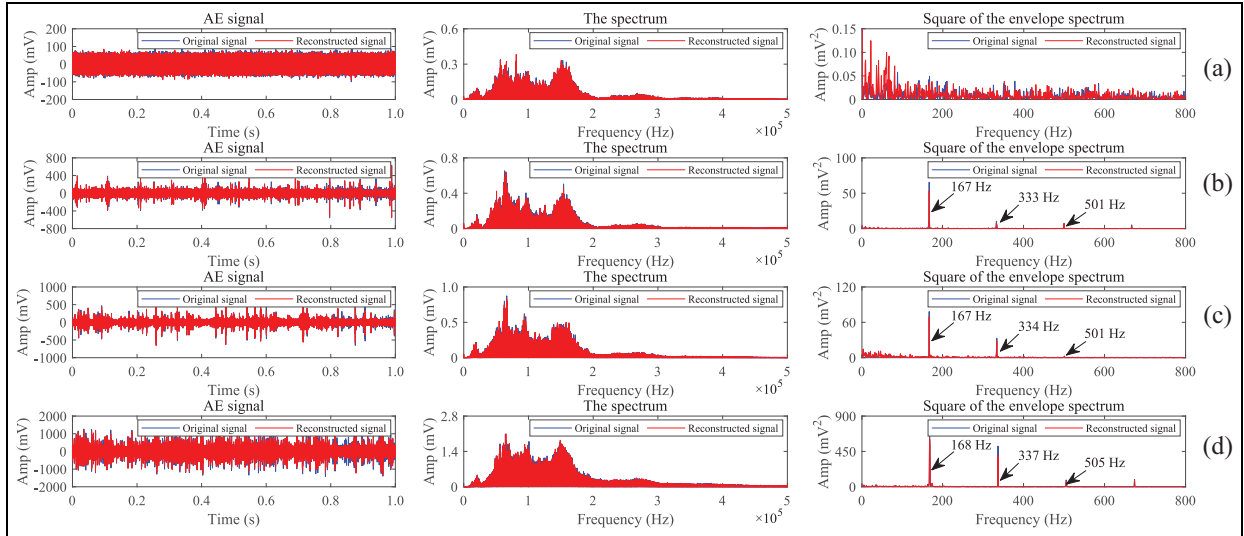


**Figure 17.** Reconstruction results of AE signal of bearings with different degrees of damage: (a) bearing A, (b) bearing B, (c) bearing C, and (d) bearing D. AE: acoustic emission.

Then the energy retention property can be described as follows:

$$|\hat{E} - E| < Q \quad (25)$$

where  $Q$  is a very small constant.

According to the energy retention property, the energy in the compression domain is almost equal to the energy in the time domain. Although the

compression domain energy characterizes the overall strength of the AE signal over a period, it cannot comprehensively evaluate the AE signal and the damage state of the bearings from multiple aspects. Therefore, amplitude, root mean square (RMS), and average signal level (ASL) are introduced to achieve a comprehensive evaluation. The amplitude mainly reflects the strength of the AE signal at a certain moment, while the RMS and ASL reflect the activity of the AE signal over a period of time. Based on ten groups of AE signals with a sampling time of 1 s, the statistics on average values of characteristic parameters of bearings with different damage levels are shown in Table 3.

The characteristic parameters in Table 3 describe different statistical features of the AE signal. They are not completely independent but are correlated to a certain extent. Therefore, to establish a comprehensive index that can reliably evaluate the bearing damage state, the principal component analysis (PCA) method is used to determine the principal components and consequently construct the DSCEI of the high-speed train bearings. The results of PCA are shown in Figure 18. For standardized data, the variance of each original variable is 1. If a principal component has an eigenvalue less than 1, it indicates that it explains less variance in the data than an individual original variable.<sup>41</sup> Therefore, the first principal component ( $PCF_1$ ) with eigenvalue greater than 1 is selected, as shown in Equation (26).

$$PCF_1 = 0.20\varpi_1 + 0.43\varpi_2 + 0.51\varpi_3 + 0.52\varpi_4 + 0.49\varpi_5 \quad (26)$$

where  $\varpi_i (i=1, 2, \dots, 5)$  is the standardized index of parameters.

Variance contribution ratio  $W_i$  is defined as shown in Equation (27):

$$W_i = \lambda_i / \sum_{j=1}^p \lambda_j \quad (27)$$

where  $W_i$  is variance contribution ratio,  $\lambda_i$  is the eigenvalue of the  $i$ th principal component, and  $p$  is the total number of principal components.

Based on the variance contribution ratio, the DSCEI is obtained as in Equation (28).

$$DSCEI = 0.73PCF_1 \quad (28)$$

According to the DSCEI, the standardized data in Table 3 are substituted into the calculation to obtain the comprehensive score of the bearing damage state, as shown in Figure 19. With the increase in high-speed train running speed and the aggravation of bearing damage, the scores of bearing damage state are higher with notable differences, indicating the accuracy of the DSCEI and its feasibility in the quantitative analysis of bearing faults.

The performance of the DSCEI is evaluated by comparing it against two commonly used fault damage indices, namely the kurtosis index (KI)<sup>42</sup> and permutation entropy index (PEI).<sup>43</sup> First, the per unit time AE data at 300 km/h speed is processed, and the values of the DSCEI, PEI, and KI are obtained. The results are then normalized to the maximum value. Figure 20 illustrates the results of the three bearings with different damage levels. The DSCEI is stable and increases gradually with the deepening of bearing damage. By contrast, the KI not only fluctuates with high intensity but also has no monotonicity. Although the value of the PEI is stable, changes in bearing damage do not result in any notable trend.

The stability of the indices is further evaluated by calculating their standard deviations. The results are illustrated in Figure 21. For each bearing, KI exhibits the largest standard deviation. Although the PEI

**Table 3.** Characteristic parameters of bearings with different defects under different running speeds.

Defect level	Running speed (km/h), $x_1$	Amplitude (dB), $x_2$	RMS (mV), $x_3$	ASL (dB), $x_4$	Compressed domain energy, $x_5$
No defect	200	75.48	18.07	83.14	3.26e8
	250	76.57	26.87	86.59	7.23e8
	300	79.12	34.51	88.76	1.19e9
Minor defect	200	89.96	27.35	86.07	7.47e8
	250	91.07	41.26	89.97	1.71e9
	300	91.70	59.83	92.91	3.58e9
Moderate defect	200	90.59	35.92	87.82	1.29e9
	250	93.46	50.91	90.88	2.59e9
	300	94.56	66.19	93.08	4.37e9
Senior defect	200	97.30	117.48	98.16	1.38e10
	250	98.05	143.22	100.07	2.05e10
	300	99.10	174.39	101.72	3.06e10

RMS: root mean square; ASL: average signal level.

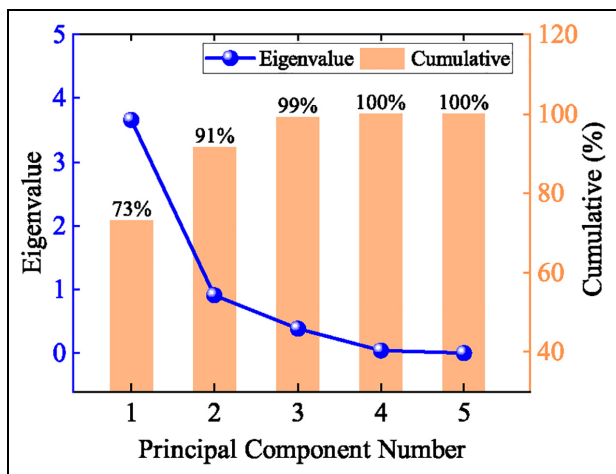


**Figure 18.** Results of PCA. PCA: principal component analysis.

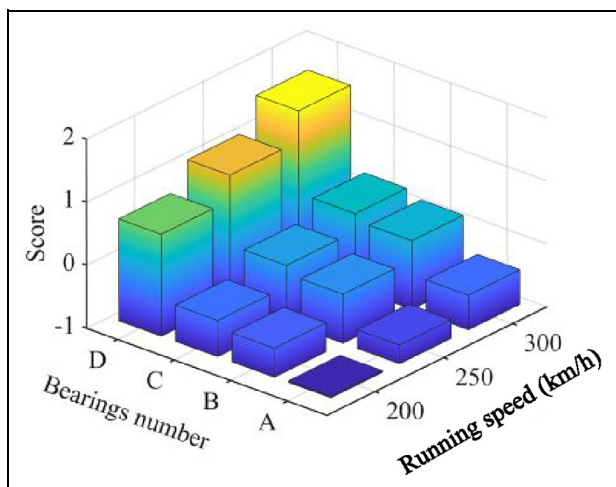


**Figure 19.** DSCEI of bearings with different damages. DSCEI: damage state comprehensive evaluation index.

consistently exhibits the smallest standard deviation, its value does not exhibit a significant trend. The standard deviation of the DSCEI is considerably smaller than that of KI and slightly larger than that of PEI, indicating a sound stability. A comparative analysis

reveals that compared to the PEI and KI, the DSCEI not only exhibits good stability but also provides better tendency and monotonicity, making it more suitable for the quantitative analysis of bearing damage in high-speed trains.

The characteristic parameters vary under different test conditions. Therefore, when applying DSCEI to other applications, preexperiments could be performed first to obtain the laws of the damage signal characteristic parameters. Second, DSCEI primarily evaluates the characteristic parameter changes of the same sensor at different stages, which help to reduce the impact of different sensor test conditions on the damage quantification results. In addition, the weights calculated by PCA in DSCEI are not fixed but flexible and variable in different scenarios, and the reliability of DSCEI gradually increases with the increase of monitoring data samples.

In summary, when the proposed method is applied in the field, the AE signal at current moment is acquired and compressed, and the aforementioned characteristic parameters are extracted to calculate the DSCEI. The compressed data and the characteristic parameters can be transmitted by wired or wireless, enabling fault diagnosis with low computational resources. The AE signal can be reconstructed based on the learning dictionary and ASFBP at the receiver terminal. Moreover, the frequency domain analysis can further improve the reliability of fault diagnosis and performance evaluation.

## Conclusions

In this article, the adaptive thresholds applicable to ASFBP and the bearing health state assessment method for high-speed trains are established. The adaptive dynamic thresholds account for the reconstruction residuals and atom quality (correlation) distribution law. This not only enables ASFBP to adaptively select and remove atoms without any step conditions but also substantially improves reconstruction accuracy and speed. ASFBP demonstrates the minimum RE compared to other two-stage reconstruction methods at

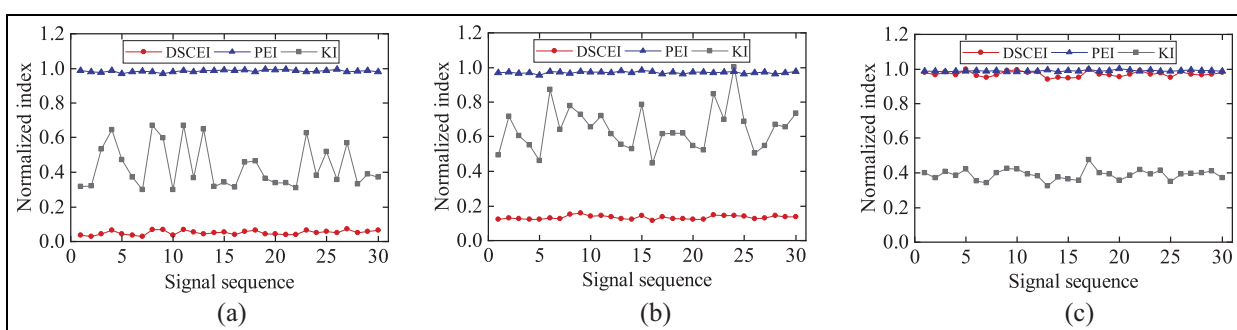


**Figure 20.** Normalized index of per time signal: (a) bearing B, (b) bearing C, and (c) bearing D.

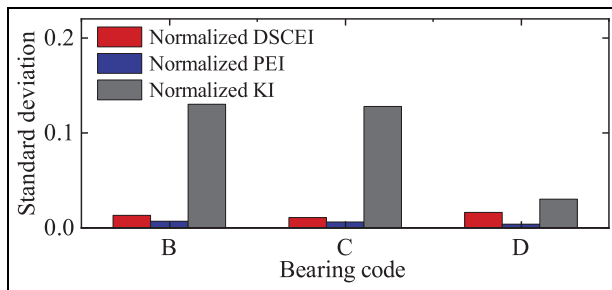


**Figure 21.** Standard deviation of normalized indices of different damaged bearings.

different compression rates. The VSFBP exhibits superior atom selection performance compared to previously reported two-stage reconstruction methods, enhancing the reconstruction performance. With an experimental AE signal length of 4000 and a compression rate of 0.6, the average RE and running time of ASFBP are 32% and 57 s, respectively. Furthermore, the reconstruction accuracy and speed improve by approximately 10% and three times, respectively, compared with VSFBP. Moreover, the coefficient of variation of reconstruction speed of ASFBP is 5.3%, which is smaller than 36.6% of VSFBP, indicating that ASFBP demonstrates a highly stable reconstruction speed.

A hit time parameter model is established based on the characteristics of bearing damage AE signal of high-speed trains, as a guidance for designing the initial dictionary length of AE signal. In addition, a DSCEI is constructed based on the compression-domain energy parameter and the AE time-domain hit parameters. Compared with the KI and the PEI, the DSCEI demonstrates a better tendency and stability in the quantitative evaluation of high-speed train bearing damage state. Finally, the validity and stability of the adaptive dynamic thresholds and state assessment method are verified by testing the AE signal of bearings with different damage levels at various speeds under complex conditions resembling real high-speed train operations. The proposed technique can enable effective data compression reconstruction and fault diagnosis. Overall, the findings of this study provide valuable insights for real-time analysis of high-speed trains and other industrial bearings based on CS and AE. In future, advanced machine learning algorithms will be utilized to construct more complete dictionaries to further improve the reconstruction performance of the ASFBP method under strong noise conditions.

### Author contributions

Defu Han has involved in methodology, software, writing—original draft. Hongyuan Qi has involved in conceptualization and data curation. ShuangXin Wang has involved in

validation. Dongming Hou has involved in data curation and validation. Cuiping Wang has involved in formal analysis.

### Declaration of conflicting interests

The author(s) declared no potential conflicts of interest with respect to the research, authorship, and/or publication of this article.

### Funding

The author(s) disclosed receipt of the following financial support for the research, authorship, and/or publication of this article: This research is supported by the Fundamental Research Funds for the Central Universities (no. 2023YJS133) and the project from CRRC QINGDAO SIFANG CO., Ltd (no. M19L01500). The authors sincerely thank all the reviewers for the valuable comments that greatly helped to improve the manuscript.

### ORCID iD

Hongyuan Qi <https://orcid.org/0000-0001-8929-214X>

### References

- Qi H, Han D, Hou D, et al. A novel acoustic emission sensor design and modeling method for monitoring the status of high-speed train bearings. *Struct Health Monit* 2023; 22(6): 3761–3784.
- Li C, Luo K, Yang L, et al. A zero-shot fault detection method for UAV sensors based on a novel CVAE-GAN model. *IEEE Sens J* 2024; 24(12): 1–1.
- Man J, Dong H, Yang X, et al. GCG: graph convolutional network and gated recurrent unit method for high-speed train axle temperature forecasting. *Mech Syst Signal Process* 2022; 163: 108102.
- Hou D, Qi H, Wang C, et al. High-speed train wheel set bearing fault diagnosis and prognostics: fingerprint feature recognition method based on acoustic emission. *Mech Syst Signal Process* 2022; 171: 108947.
- Wang J, Ma X, Qiu Q, et al. A hybrid inspection-replacement policy for multi-stage degradation considering imperfect inspection with variable probabilities. *Reliab Eng Syst Safe* 2023; 241: 109629.
- Mahajan H and Banerjee S. Acoustic emission source localisation for structural health monitoring of rail sections based on a deep learning approach. *Meas Sci Technol* 2023; 34(4): 044010.
- Yoshioka T and Fujiwara T. Application of acoustic emission technique to detection of rolling bearing failure. *Am Soc Mech Eng* 1984; 14(1): 55–76.
- Eftekharnajad B, Carrasco MR, Charnley B, et al. The application of spectral kurtosis on acoustic emission and vibrations from a defective bearing. *Mech Syst Signal Process* 2011; 25(1): 266–284.
- Mahajan H and Banerjee S. Quantitative investigation of acoustic emission waveform parameters from crack opening in a rail section using clustering algorithms and advanced signal processing. *Sensors* 2022; 22(22): 8643.

10. Hou D, Qi H, Luo H, et al. Comparative study on the use of acoustic emission and vibration analyses for the bearing fault diagnosis of high-speed trains. *Struct Health Monit* 2022; 21(4): 1518–1540.
11. Kannan V, Dao DV and Li H. An information fusion approach for increased reliability of condition monitoring with homogeneous and heterogeneous sensor systems. *Struct Health Monit* 2023; 22(3): 1601–1612.
12. Donoho DL. Compressed sensing. *IEEE Trans Inf Theory* 2006; 52(4): 1289–1306.
13. Candès EJ and Tao T. Decoding by linear programming. *IEEE Trans Inf Theory* 2005; 51(12): 4203–4215.
14. Khan I, Xu Y, Kar S, et al. Compressive sensing and morphology singular entropy-based real-time secondary voltage control of multiarea power systems. *IEEE Trans Ind Inform* 2018; 15(7): 3796–3807.
15. Peng Y, Qiao W and Qu L. Compressive sensing-based missing-data-tolerant fault detection for remote condition monitoring of wind turbines. *IEEE Trans Ind Electron* 2021; 69(2): 1937–1947.
16. Tang Z, Bao Y and Li H. Group sparsity-aware convolutional neural network for continuous missing data recovery of structural health monitoring. *Struct Health Monit* 2021; 20(4): 1738–1759.
17. Bao Y, Tang Z and Li H. Compressive-sensing data reconstruction for structural health monitoring: a machine-learning approach. *Struct Health Monit* 2020; 19(1): 293–304.
18. Liu C, Wu X, Mao J, et al. Acoustic emission signal processing for rolling bearing running state assessment using compressive sensing. *Mech Syst Signal Process* 2017; 91: 395–406.
19. Bao Y, Shi Z, Wang X, et al. Compressive sensing of wireless sensors based on group sparse optimization for structural health monitoring. *Struct Health Monit* 2018; 17(4): 823–836.
20. Sawant S, Banerjee S and Tallur S. Performance evaluation of compressive sensing based lost data recovery using OMP for damage index estimation in ultrasonic SHM. *Ultrasonics* 2021; 115: 106439.
21. Cheng Z and Lu Z. Two novel reconstruction methods of sparsity adaptive adjustment for road roughness compressive signal based on I-SA and GSM. *Mech Syst Signal Process* 2022; 171: 108915.
22. Zhang GM, Zhang CZ and Harvey DM. Sparse signal representation and its applications in ultrasonic NDE. *Ultrasonics* 2012; 52(3): 351–363.
23. Kim T, Lee G and Youn BD. PHM experimental design for effective state separation using Jensen–Shannon divergence. *Reliab Eng Syst Safe* 2019; 190: 106503.
24. Mallat SG and Zhang Z. Matching pursuits with time-frequency dictionaries. *IEEE Trans Signal Process* 1993; 41(12): 3397–3415.
25. Tropp JA and Gilbert AC. Signal recovery from random measurements via orthogonal matching pursuit. *IEEE Trans Inform Theory* 2007; 53(12): 4655–4666.
26. Wang J, Kwon S and Shim B. Generalized orthogonal matching pursuit. *IEEE Trans Signal Process* 2012; 60(12): 6202–6216.
27. Needell D and Vershynin R. Uniform uncertainty principle and signal recovery via regularized orthogonal matching pursuit. *Found Comput Math* 2009; 9: 317–334.
28. Li F, Hong S, Gu Y, et al. An optimization-oriented algorithm for sparse signal reconstruction. *IEEE Signal Process Lett* 2019; 26(3): 515–519.
29. Dai W and Milenkovic O. Subspace pursuit for compressive sensing signal reconstruction. *IEEE Trans Inform Theory* 2009; 55(5): 2230–2249.
30. Needell D and Tropp JA. CoSaMP: iterative signal recovery from incomplete and inaccurate samples. *Appl Comput Harmon A* 2009; 26(3): 301–321.
31. Su L, Tan S, Qi Y, et al. An improved orthogonal matching pursuit method for denoising high-frequency ultrasonic detection signals of flip chips. *Mech Syst Signal Process* 2023; 188: 110030.
32. Do TT, Gan L, Nguyen N, et al. Sparsity adaptive matching pursuit algorithm for practical compressed sensing. In *42nd Asilomar conference on signals, systems and computers*, Pacific Grove, CA, 26–29 October 2008, pp. 581–587. Piscataway, NJ: IEEE Press.
33. Wang C, Zhang Y, Sun L, et al. Improved sparsity adaptive matching pursuit algorithm based on compressed sensing. *Displays* 2023; 77: 102396.
34. Karahanoglu NB and Erdogan H. Compressed sensing signal recovery via forward–backward pursuit. *Digit Signal Process* 2013; 23(5): 1539–1548.
35. Aziz A, Osamy W, Khedr AM, et al. Iterative selection and correction based adaptive greedy algorithm for compressive sensing reconstruction. *J King Saud Univ Comput Inf Sci* 2022; 34(3): 892–900.
36. Pan Z, Meng Z, Zhang Y, et al. High-precision bearing signal recovery based on signal fusion and variable step-size forward-backward pursuit. *Mech Syst Signal Process* 2021; 157: 107647.
37. Lv C, Ma J, Liu H, et al. *Fault diagnosis and prognostics based on cognitive computing and geometric space transformation*. Beijing, China: National Defense Industry Press, 2021.
38. Chang YH, Wang W, Chang JY, et al. Compressed sensing for OMA using full-field vibration images. *Mech Syst Signal Process* 2019; 129: 394–406.
39. Aharon M, Elad M and Bruckstein A. K-SVD: an algorithm for designing overcomplete dictionaries for sparse representation. *IEEE Trans Signal Process* 2006; 54(11): 4311–4322.
40. Du Z, Chen X, Zhang H, et al. Learning collaborative sparsity structure via nonconvex optimization for feature recognition. *IEEE Trans Ind Inform* 2017; 14(10): 4417–4430.
41. Jolliffe IT. *Principal component analysis*. New York, NY: Springer, 2002.
42. Lei Y, Li N and Lin J. A new method based on stochastic process models for machine remaining useful life prediction. *IEEE Trans Instrum Meas* 2016; 65(12): 2671–2684.
43. Tian Y, Wang Z and Lu C. Self-adaptive bearing fault diagnosis based on permutation entropy and manifold-based dynamic time warping. *Mech Syst Signal Process* 2019; 114: 658–673.